PAPER

The effect of rigid electron rotation on the Grad–Shafranov equilibria of a class of FRC devices

IOP Publishing | International Atomic Energy Agency Nuclear Fusion

Nucl. Fusion **61** (2021) 086023 (14pp) https://doi.org/10.1088/1741-4326/ac0f96

The effect of rigid electron rotation on the Grad–Shafranov equilibria of a class of FRC devices

C.P.S. Swanson[1,2,*] **and S.A. Cohen**[2]

[1] Princeton Fusion Systems, Plainsboro, NJ, United States of America
[2] Princeton Plasma Physics Laboratory, Princeton, NJ, United States of America

E-mail: cswanson@pppl.gov

Received 19 March 2021, revised 4 June 2021
Accepted for publication 29 June 2021
Published 16 July 2021

Abstract

Rigid electron rotation of a Rotamak-FRC produces a pressure flux function that is more peaked than the Solov'ev flux function. This paper explores the implications of this peaked pressure flux function, including the isothermal case, which appear when the temperature profile is broader than the density profile, creating both benefits and challenges to a Rotamak-FRC based fusion reactor. In this regime, the density distribution becomes very peaked, enhancing the fusion power. The separatrix has a tendency to become oblate, which can be mitigated by flux conserving current loops. Plasma extends outside the separatrix, notably in the open field line region. This model does not apply to very kinetic FRCs or FRCs in which there are significant ion flows, but it may have some applicability to their outer layers.

Keywords: nuclear fusion, field-reversed configuration, magnetohydrodynamics, Grad Shafranov, rigid rotor

(Some figures may appear in colour only in the online journal)

1. Introduction

Rotamak-FRCs are plasma physics experimental devices in which electron current is driven by an externally-imposed rotating magnetic field (RMF) [1]. They are also called RMF-driven FRCs. Interest in this configuration of plasma arises from its favorable properties for scaling into a nuclear fusion reactor, particularly a compact one [2–6]. The favorable properties include: high plasma β, maximizing the plasma pressure for a given magnetic field; low internal field, allowing high-temperature and advanced fuels; and a simple, compact, and efficient method of heating and current drive in the form of the RMF system. RMF current drive dates to the 1960s [7]. There have been several Rotamak-FRC experiments operating since the 1990s [6, 8–11]. An existing example is the Princeton field-reversed configuration 2 (PFRC-2) experiment at the Princeton Plasma Physics Laboratory (PPPL) [12].

The name Rotamak was coined by Jones [8, 10]. Originally, the 'reversed field' of the 'field-reversed configuration' (FRC) referred to the θ-pinch method of formation, in which the bias field was quickly ramped and reversed to drive plasma current. FRC now more typically refers to the plasma configuration, regardless of how it was produced.

In fully penetrated Rotamak-FRCs, the current drive is assumed to be due to electrons rotating in synchrony with the applied external RMF while the ions are stationary [1, 10, 13–16]. There is also speculation that FRCs that are not driven by RMF will still rotate synchronously due to collisional effects [17]. This argument extends to both electrons and ions, although they will rotate at different rates. RMF-synchronous electron rotation has been observed in experiments [18] and PIC (kinetic) simulation [19].

A simplified (no B_t) Grad–Shafranov model is often used to predict and reconstruct the MHD equilibria of these plasma configurations [20, 21]. While many modern analyses assume a Solov'ev [21] pressure flux function, with $P \propto \Psi$ (pressure linear in flux) [22–24], it has been known since 1982

* Author to whom any correspondence should be addressed.

that the Solov'ev linear pressure flux function is the *least* steep pressure flux function consistent with rigid rotation, and that more realistic flux functions have a higher power law, $P \propto \Psi^N$, $N \geqslant 1$ [25–27] or even an exponential relationship, $P \propto e^{\Psi/\Psi_0}$ [17, 28–32]. The well-known rigid rotor 1D radial pressure profile $P(r), B(r)$ implicitly assumes this pressure flux function.

Where these steeper pressure flux functions have been used to numerically generate equilibria, it has predominantly been for the purpose of fitting to experimental measurements. In this context, the implications of this steeper pressure flux function on fusion reactor design have not been explored in detail.

The Grad–Shafranov equation has also been used to model FRC equilibria with more complex, multi-parameter pressure flux functions that do not include rigid rotor effects [33, 34].

In section 2, we motivate these calculations by summarizing the properties of a Rotamak-FRC-based fusion reactor. In section 3, we introduce the geometry of the FRC and FRC-related terminology and conventions. In section 4, we introduce the calculation, its assumptions, and its applicability to experiment and reactors. In section 5, we will derive the flux functions to be inserted into the Grad–Shafranov solver that are required by the condition of rigid electron rotation. In section 6, we will discuss the likely values of the free parameters that are defined in section 5, the likely relative peakedness of the density and temperature profiles. In section 7, we discuss the solver which produces self-consistent MHD equilibria from the equations in section 5. In section 8, we will discuss the results of these MHD equilibria. In section 9, we will conclude with a discussion of these results and their effect on the future design of Rotamak-FRC based fusion reactors.

Table 1. Parameters of the PFRC-based fusion reactor, called the DFD when considered as a rocket for in-space propulsion.

Parameter	Quantity
Electron temperature (T_e)	50 keV
Electron density (n_e)	4×10^{14} (cm^3)
RMF angular frequency (ω_{RMF})	$2\pi \times 10^6$ rad s^{-1}
RMF field magnitude (B_{RMF})	200 Gauss
Vacuum field (B_0)	5 T
Plasma radius (r_s)	25–30 cm
Plasma length (L)	1–10 m
Fusion power (P_{fus})	1–10 MW
Fusion fuel	D-^{3}He
RMF power (P_{RMF})	100 kW–1 MW
RMF parity	Odd (RMF$_o$)
Reactor diameter	1–2 m
Reactor mass	1–10 tons

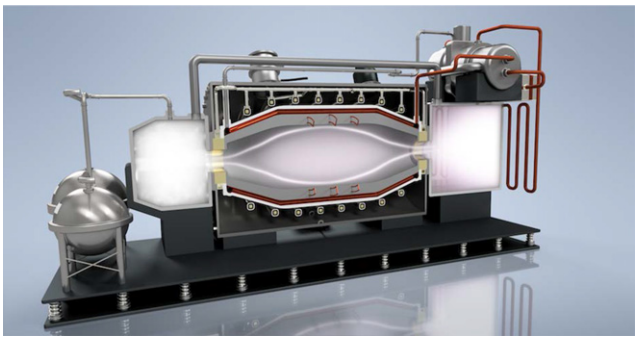

Figure 1. A rendering of a PFRC-based Rotamak-FRC fusion reactor. The FRC plasma (center) is surrounded by three RMF antennae, a vacuum vessel, and a solenoidal magnet array. A heat engine in the upper-righthand corner generates useful electricity. Image used courtesy of Princeton fusion systems (PFS).

2. Rotamak-FRC fusion reactors

It is beyond the scope of this paper to describe a Rotamak-FRC-based fusion reactor, or argue the existence of a favorable design point. For discussion of such a reactor, see the 'path to fusion' section of Slough and Miller [5], and descriptions of a Rotamak-FRC-based fusion rocket in two papers by Cohen *et al* [2, 4]. Both of these sources discuss the possibility of using FRCs' unique strengths to produce in-space rocket engines, a path also espoused by Wurden *et al* [3].

The in-space application highlights the unique strength of the Rotamak-FRC compared to other magnetic fusion energy concepts. The FRC has a high plasma β, which maximizes the plasma pressure for a given magnetic field. This also maximizes the fusion power for a given magnet system mass. The low internal field of the FRC also allows advanced fuels such as D-^{3}He to be considered, as it limits synchrotron radiation emission, creating a more favorable scaling at high plasma temperature. The RMF system is a simple, compact, and efficient method of heating and current drive.

For specificity, we tabulate example values of plasma parameters of the Rotamak-FRC reactor described in Cohen *et al* [2, 4], which is called the direct fusion drive (DFD) and is supported by the PFRC-2 experiment at the PPPL [12]. These parameters are tabulated in table 1. We note the favorable reactor size and specific power (P_{fus}/mass) enabled by the Rotamak-FRC configuration.

A Rotamak-FRC fusion reactor concept typically consists of: a solenoidal vacuum field system (typically superconducting and flux conserving), a vacuum vessel and pumping system, an FRC formation and sustainment system (RMF), a fueling system (neutral beam injection or plasmoid injection), and a heat engine for electricity generation. See a rendering in figure 1.

Existing large, short-pulse Rotamak-FRC experiments have measured Bohm-like or microturbulence-driven transport, which is unfavorable to fusion reactor parameters [35]. This high level of particle transport is attributed to saturation of the lower hybrid drift wave (LHD). The PFRC-based reactor concept is linearly stable to LHD [2]. Transport is assumed to be near-classical, as has been theorized [36] and found of the fast ions in the TAE energy C2 experiment [37].

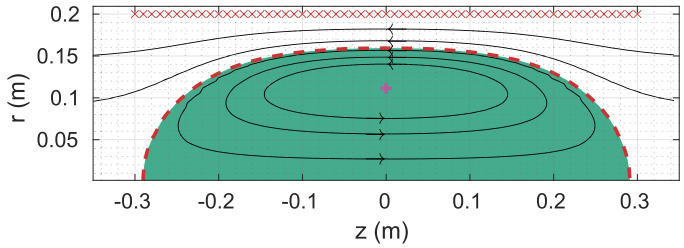

Figure 2. Anatomy of a typical FRC. Black lines: $\vec{B}$-field lines, or equivalently contours of constant flux Ψ. Red $\times$ s: external solenoidal magnets. Green shaded region: closed field line region. White shaded region: open field line region. Red dashed line: the separatrix. Magenta $+$: the o-point null. Radially inward of the null, the magnetic field is in the $+\hat{z}$ direction as indicated by the arrows. Radially outward of the null, the magnetic field is in the $-\hat{z}$ direction.

3. Anatomy of an FRC

This section introduces the geometry of the FRC. A toroidal/azimuthal cross section (r, z) of an example FRC is shown in figure 2. Like most FRCs considered for fusion reactors, this example FRC is prolate rather than oblate, with an elongation (half-length/radius) of 2.

The FRC contains current $\vec{j} = j_\phi \hat{\phi}$ only in the azimuthal direction, and a magnetic field $\vec{B}$ only in the $\hat{r}$ and $\hat{z}$ directions. There is no toroidal/azimuthal magnetic field. The magnetic field is composed of externally applied vacuum field and self-generated plasma field generated by j_ϕ.

The FRC is divided into two volumes. The closed field line volume corresponds to the area shaded green in the figure. In this volume, magnetic field lines are closed and particles are nominally trapped. The open field line volume corresponds to the area shaded white in the figure. In this volume, magnetic field lines exit the vacuum vessel, so particles following a field line exit the reaction volume and hit the wall. However, if the FRC is embedded in a magnetic mirror, this loss of particles can be mitigated by mirror confinement. The surface between these two volumes is called the separatrix and corresponds to the red dashed line in the figure.

The FRC has a line at which the magnetic field is zero. This is called the o-point null line, and corresponds to the magenta $+$ in the figure. The pressure profile $P(r, z)$ has a maximum at this point. Inward of the null, the magnetic field faces one axial direction, by convention $+\hat{z}$ as in the figure. Outward of the null, the magnetic field faces the other axial direction, $-\hat{z}$.

In an ideal MHD equilibrium, the pressure gradient $-\vec{\nabla}P$ is balanced by the Lorentz force $\vec{j} \times \vec{B}$. Because of this relationship between pressure, magnetic field, and current, the magnetic and pressure profiles assume a self-consistent shape found using the Grad–Shafranov equation [20, 21].

4. Summary of calculation and applicability

This paper will calculate the self-consistent shape of FRC equilibria assuming ideal MHD, axisymmetry, and rigid electron rotation (ω_e constant). This calculation is described in section 5. A specific functional form of the pressure-dependence of density and temperature is assumed, $n_e/n_0 = (P/P_0)^\mu, T/T_0 = (P/P_0)^{1-\mu}$, where μ is a number between 0 and 1. As we will see in section 5, these assumptions imply a specific functional form of the pressure flux-function used in the Grad–Shafranov Equation, $P(\Psi)$ [20, 21]. This functional form is either a simple power law $P \propto \Psi^N$ for the non-isothermal case $0 \leqslant \mu < 1$, or a simple exponential $P \propto e^{\Psi/\Psi_c}$ for the isothermal case $\mu = 1$.

Notably, the MHD calculation herein assumes an isotropic pressure, which is of arguable validity outside the separatrix in the open-field-line region. The mirror confinement and its associated loss via the loss cone is completely absent from this model.

We have not performed analysis of the stability of these equilibria. No kinetic effects are present. No ion flow is assumed. In an FRC-based compact fusion reactor, these effects may be important, as the ion thermal gryoradius is significant compared to the size of the plasma.

Models show that the assumption that electrons rotate rigidly is good in the limiting case of completely penetrated RMF field. Indeed, complete penetration is only possible when the electrons rotate synchronously with the RMF, $\omega_e = \omega_{RMF}$. In the more general case that the RMF magnitude is finite, the plasma is collisional, and/or the plasma radius is large, the electrons do not rotate synchronously with the RMF but will still rotate rigidly, $\omega_e < \omega_{RMF}$ [1, 10, 13–16]. Rigid electron rotation is found in experiment on the TCS-U experiment [18, 38], MHD simulation [14, 16], and PIC (kinetic) simulation [19].

Rostoker and Qerushi argue that FRCs will rotate rigidly regardless of whether RMF is present, for example if the FRC is formed via θ-pinch. They argue this due to collisional equilibration, stating: 'the only drifted Maxwellians that satisfy the Vlasov equation for systems with cylindrical symmetry are rigid rotors' [17].

Subsynchronous rigid rotation ($\omega_e < \omega_{RMF}$) can also be described as incomplete RMF penetration [1, 10, 13–16]. Hugrass uses this penetration length: [13, 14]

$$\delta_{RMF} = \frac{\omega_{ce,RMF}}{\nu_{e,i}} \sqrt{\frac{\eta}{\omega_{RMF}\mu_0}}, \tag{1}$$

where δ_{RMF} is the penetration depth of the RMF field, $\omega_{ce,RMF}$ is the electron gyrofrequency in the RMF field, $\nu_{e,i}$ is the electron–ion collision time, η is the resistivity of the plasma, ω_{RMF} is the angular frequency of the RMF, and μ_0 is the magnetic permeability of free space.

Using the Spitzer resistivity for η, we find the following dependency:

$$\delta_{\mathrm{RMF}} = \omega_{\mathrm{ce,RMF}} \sqrt{\frac{3\alpha_{\mathrm{S}}}{2^{9/2}\pi^{3/2}} \frac{1}{\omega_{\mathrm{RMF}}} \frac{(T_{\mathrm{e}}/m_{\mathrm{e}}c^2)^{3/2}}{Zn_{\mathrm{e}}^2 r_{\mathrm{e}}^3 c \ \ln \Lambda}} \propto n^{-1}, \quad (2)$$

where $\alpha_{\mathrm{S}} \approx 0.51$ is the Spitzer correction to the DC resistivity, $m_{\mathrm{e}}/c^2 \approx 511 \times 10^3$ eV is the electron rest energy, $r_{\mathrm{e}} \approx 2.82 \times 10^{-13}$ cm is the classical electron radius, and $c \approx 3.00 \times 10^{10}$ cm s^{-1} is the speed of light in a vacuum.

Using example parameters in table 1 of $T_{\mathrm{e}} = 50$ keV, $n_{\mathrm{e}} = 4 \times 10^{14}$ 1/cm^3, $\omega_{\mathrm{RMF}} = 2\pi \times 10^6$ rad s^{-1}, we find that a B_{RMF} as low as 16 Gauss is sufficient for penetration length of $\delta_{\mathrm{RMF}} = 50$ cm. This is long compared to the FRC radius of 25 cm, so RMF penetration can be considered complete at the design B_{RMF} amplitude of 200 G. Penetration sets one criterion on the minimum B_{RMF} amplitude, but power deposition and transport sets a more stringent one in the case of the design point tabulated. Hence, 200 G rather than 16 G.

A full discussion of RMF current drive is beyond the scope of this paper, but note that a very small RMF field, 200 G, can reverse a vacuum field two orders of magnitude larger, 5 T. An intuitive justification for this is often formulated in terms of torques, by a balance of RMF torque and collisional torque between the electrons and background ions. In a reactor-relevant regime, collisionality is small and it does not take a very large RMF torque to balance the small collisional drag torque. For a more complete discussion, see Hoffman *et al* [1].

Much discussion has been given to the possibility that the ions will collisionally spin up and become synchronous with the electrons [39]. This would cancel out the FRC current and no plasma would be confined. It is claimed that existing low-temperature experiments have ion populations which share momenta with the neutral gas populations and the wall, which act as ion momentum sinks. Suggestions for reactor-scale solutions include ion momentum injection via a neutral beam and using the RMF to couple to the ions, either alone or in addition to an electron RMF signal.

5. The pressure flux functions produced by rigid rotation

In this section we will derive the pressure flux function to substitute into the Grad–Shafranov equation [20, 21]. The Grad–Shafranov model has the pressure flux function as a free parameter, but as we will see here, the condition of rigid electron rotation implies a functional form.

The central assumption of this model is that synchronous-electron current (equation (5)) is the diamagnetic current (equation (3)), that is that $\vec{j} \times \vec{B}$ balances $\vec{\nabla} P$. The net effect of RMF is that it forces density to migrate across field lines until the pressure profile is such that the diamagnetic electron velocity rotates synchronously.

5.1. Diamagnetic current condition, MHD equilibrium

We assume an ideal axisymmetric MHD equilibrium and that the plasma pressure at any given point is a function only of the enclosed flux, $P(\Psi(r,z))$. The equilibrium equation is simplified when it is assumed that there is no toroidal magnetic field.

The equilibrium condition is

$$\vec{j} \times \vec{B} = \vec{\nabla} P. \quad (3)$$

By assuming axisymmetry, no toroidal field, and an isotropic pressure flux function $P(\Psi)$, this equation becomes:

$$j_\phi = 2\pi r \partial_\Psi P, \quad (4)$$

where ϕ is the toroidal or azimuthal direction, $P = \Sigma nT$ is the plasma pressure, r is the radial coordinate, $\Psi(r,z) = \int_0^r \mathrm{d}r' 2\pi r B_z(r',z)$ is the enclosed flux at point (r,z), $\partial_\Psi P$ is the derivative of the plasma pressure P with respect to the magnetic flux Ψ. Ψ has not been normalized by 2π as is sometimes the custom.

Equation (4) is an intermediate step in the derivation of the Grad–Shafranov equation [20, 21].

5.2. Rigid rotor current condition

We assume that the current is due to all electrons rigidly rotating in synchrony (rigid rotation). The electron current is:

$$j_\phi = e n_{\mathrm{e}} r \omega_{\mathrm{e}}, \quad (5)$$

where ω_{e} is the angular frequency of the azimuthal electron rotation, assumed to be uniform throughout the plasma, and $\omega_{\mathrm{e}} \leqslant \omega_{\mathrm{RMF}}$. In order to compute $P(\Psi)$, we will substitute equation (5) into equation (4):

$$2\pi r \partial_\Psi P = e n_{\mathrm{e}} r \omega_{\mathrm{e}}. \quad (6)$$

If instead the current drive were due to ions rotating against stationary electrons, an ion momentum term would have to be added to the Grad–Shafranov equation. These results still hold (with subscripts e, i transposed) in the regime that $m_{\mathrm{i}} r^2 \omega_{\mathrm{i}}^2 \ll T_{\mathrm{i}}$.

We will now discuss the relationship between density, temperature, and pressure:

$$n_{\mathrm{i}} T_{\mathrm{i}} + n_{\mathrm{e}} T_{\mathrm{e}} = nT = P, \quad (7)$$

where

$$n_{\mathrm{e}} = n_{\mathrm{i}} = n \quad (8)$$

and

$$T = T_{\mathrm{i}} + T_{\mathrm{e}} \quad (9)$$

are valid when $Z = 1$, the ion charge state is 1.

To proceed, we must make an assumption of the relative contributions of density and temperature to the pressure change. We use the common parameterization that density and temperature vary as a power law with the pressure whose exponents sum to 1:

$$n_{\mathrm{e}}/n_0 = (P/P_0)^{\mu} \quad (10)$$

$$T/T_0 = (P/P_0)^{1-\mu}, \quad (11)$$

where μ is a number between 0 and 1, and $P_0 = n_0 T_0$ are the pressure, density, and temperature at some arbitrary point. $\mu = 0$ corresponds to the constant-density case, where variation in temperature is responsible for the variation in pressure. $\mu = 1$ corresponds to the isothermal case, where variation in density is responsible for the variation in pressure.

The behavior for $\mu = 1$ must be treated differently from the behavior for $0 \leqslant \mu < 1$.

5.3. The case of $0 \leqslant \mu < 1$

This case, encompassing all situations except the isothermal, was explored by Storer in 1982 and 1983 [25, 26]. The special case of $\mu = 1/2$ was explored in detail by Donnelly *et al* in 1987 [27].

Equations (6) and (10) have the solution: [25]

$$P \propto (\Psi - \Psi_0)^{\frac{1}{1-\mu}} \tag{12}$$

$$n_e \propto (\Psi - \Psi_0)^{\frac{\mu}{1-\mu}} \tag{13}$$

$$T = \frac{1-\mu}{2\pi} e\omega_e (\Psi - \Psi_0), \tag{14}$$

where Ψ_0 is the value of the flux at the plasma-vacuum boundary, which may or not be the separatrix. $\Psi = 0$ at the separatrix.

Several interesting features are apparent:

Steep power law: equation (12) is what is substituted into equation (4) to find the Grad–Shafranov equilibrium. This is a power-law function, $P \propto \Psi^N$, $N = \frac{1}{1-\mu} \geqslant 1$. The least steep exponent is $N = 1$, the Solov'ev function, which corresponds to $\mu = 0$. This analysis indicates that the Solov'ev solution is only valid for rigid electron rotation when the density is constant, and only the temperature varies. If the density is allowed to vary at all, $N > 1$ and the pressure flux function becomes more steep. We will find in section 8 that a steep function of flux results in a pressure profile that is peaked at the magnetic axis.

The specificity of T: T, as specified in equation (14), does not have a multiplicative free parameter as P, n do in equations (12) and (13). It is always linear to the flux, and the constant of proportionality is always $\frac{1-\mu}{2\pi} e\omega_e$. For T to reach a large thermonuclear value, ω_e and Ψ must be large enough.

This analysis breaks down when $\mu = 1$. This case is discussed in section 5.4. The $\mu = 1$ case is not $T = 0$ as equation (14) would imply; rather it is T constant. In order for the $\mu = 1$ case to be the limiting case of equation (14) as $\mu \to 1$, it must also be that $\Psi_0 \to -\infty$.

Equation (14) implies that T can go to infinity as ω_e does the same. However, when $\omega_e \sim \Omega_e$, the cyclotron frequency of the electrons, then RMF no longer drives electrons and the assumption of rigid electron rotation is invalid. Equation (14) should only be considered valid for $\omega_e < \Omega_e$.

The free plasma boundary: the plasma-vacuum boundary is not necessarily the separatrix; there could be significant density in the open field line region outside the FRC. In fact this may be unavoidable, as transport of particles out of the FRC may fill this region. However, recall that it was noted in section 4 that this isotropic-pressure MHD model is not applicable in the open field line region, with its mirror confinement and loss cone. The specific profiles outside the separatrix obtained by setting $\Psi_0 < 0$ should be considered only *qualitatively* correct, not *quantitatively*.

5.4. The isothermal case, $\mu = 1$

While Storer did not consider the case that the plasma could be isothermal, $\mu = 1$, examination of this case actually precedes high-power RMF experiments. Christofilos and the Astron group modeled the Astron fusion reactor design using an isothermal rigid-rotor profile as early as the 1950s [28, 29]. The well-known rigid rotor 1D radial profile is implicitly isothermal [30, 40, 41].

These equilibria have been applied to non-RMF-driven FRC equilibria. The justification for using a rigid rotor model even when there is no RMF to drive to synchrony is often along the lines of Rostoker and Qerushi: 'the only drifted Maxwellians that satisfy the Vlasov equation for systems with cylindrical symmetry are rigid rotors' [17]. Because no RMF was assumed to drive the electrons at some angular velocity ω_e, the value of ω_e was considered a free parameter, either assumed or used to fit to experimental measurements.

Several groups have written the Grad–Shafranov equation with a pressure flux function that corresponds to the isothermal case (exponential with flux), whether or not they explicitly recognized their equation as such [17, 29, 31, 32].

Belova used the Grad–Shafranov equation with an isothermal pressure flux function to produce their starting FRC equilibria for analysis of stability [31]. Gota used the Grad–Shafranov equation with an isothermal pressure flux function to fit to experimental data [32].

In the isothermal case, equations (6) and (10) have the solution:

$$P \propto \mathrm{e}^{\Psi/\Psi_c} \tag{15}$$

$$n_e \propto \mathrm{e}^{\Psi/\Psi_c} \tag{16}$$

$$\Psi_c = \frac{2\pi T}{e\omega_e}, \tag{17}$$

where Ψ_c is a characteristic flux determined by T and ω_e. Ψ_c controls the steepness of the profiles. As Ψ_c decreases, profiles become steeper.

As a reminder, when temperature is not constant, equations (12)–(14) hold rather than equations (15)–(17). Several interesting features are apparent:

Steep pressure function: depending on the values of the factors in equation (17), equation (15) could be an extremely steep function of Ψ. As we will see in section 8, this translates into an extremely peaked pressure profile in space.

Other researchers have noted that isothermal synchronous rotation can lead to a very peaked radial density profile $n(r)$ [17, 28]. However we will discuss in section 8 that this steep profile has a tendency to be axially steep also, tightly peaked at the magnetic axis.

No plasma boundary: according to equation (16), there cannot be a plasma flux boundary outside of which the density is zero. There is always plasma outside the FRC separatrix, in the open field line region. While it was noted in section 4

that this isotropic-pressure MHD model is inapplicable in the open field line region, this finding is at least qualitatively correct: it can be understood by examining the diamagnetic drift velocity where n goes to zero as T stays finite: it is locally infinite at this point and therefore cannot obey the rigid rotation criterion.

This lack of a boundary is visible even in the well-known rigid rotor 1D radial profile, which exponentially decays to $n(r) \to 0$ but never reaches it.

Depending on the values of the factors in equation (17), the drop-off of density outside the separatrix could be either steep, in which case plasma contact with the wall could be practically mitigated, or shallow, in which case wall contact is a large effect. We will explore this behavior in section 8.

This lack of a boundary, a flux level outside which $n = 0$, explains the lack of consistency between the $\mu < 1$ pressure flux function (power law, equation (12)) to the $\mu = 1$ pressure flux function (exponential, equation (15)). The latter does not follow from simply taking the limit as $\mu \to 1$. For all $\mu < 1$, there is some flux boundary Ψ_0 outside which $T = 0$; this feature is absent in the case of $\mu = 1$.

6. Likely values of μ in experiment and reactor

The analysis presented in this paper assumes that the value of μ is known. Recall that μ is a measure of the relative peakedness of the density and temperature flux functions. At $\mu = 0$, the density is constant and the temperature is peaked. At $\mu = 1$, the temperature is constant and the density is peaked. In an experiment or a fusion reactor, several coupled processes will determine μ. A few of these processes are: transport of particles and energy, wall interaction, localized power deposition, and particle sources.

Storer fits calculated equilibria to experimental data and obtains $N = 1.6$, $\mu = 0.375$ [26]. This was a small, cool ($T_e \approx 17$ eV) Rotamak which was wall-limited [23]. Because the wall was cooled by edge contact, it is understandable that the pressure balance was determined more strongly by a temperature gradient than a density gradient ($\mu < 0.5$).

In a fully-ionized, less collisional reactor-scale plasma, the situation will change. Transport of energy tends to be significantly faster than transport of particles [42]. This will result in a density profile that is more peaked and a temperature profile that is more broad. This situation corresponds to $\mu > 0.5$. In fact, if the recycling can be kept to a negligible level, the edge of the plasma may be at thermonuclear temperatures and the plasma may be effectively isothermal [43]. Indeed, one philosophy of tokamak design holds that a hot (thermonuclear temperature) edge is beneficial to fusion reactors [44].

Gota fits calculated equilibria to experimental data, evaluating the result for three assumed pressure flux functions [32]. The functions are the Solov'ev case ($P \propto \Psi$, $\mu = 0$), the quadratic case ($P \propto \Psi^2$, $\mu = 1/2$), and the isothermal case ($P \propto e^{\Psi/\Psi_0}$), $\mu = 1$. They note that, for their experiment, the Grad–Shafranov equilibria using the three different profiles are 'almost the same'.

7. The solver: iteratively determined Grad–Shafranov equilibria

Two equations were Picard iterated to determine the self-consistent Grad–Shafranov equilibrium. One of them was equation (4), reproduced here with more explicit dependences:

$$j_\phi(r,z) = 2\pi r \partial_\Psi P(\Psi(r,z)). \tag{18}$$

The other is Ψ generated from the resulting j_ϕ, as determined from the elliptic integral Green's function of Ampere's law for flux in cylindrical coordinates:

$$\Psi(r,z) = \int \mathrm{d}r' \int \mathrm{d}z' j_\phi(r',z') G(r,z,r',z') + \Psi_\mathrm{v} + \Psi_\mathrm{FC}, \tag{19}$$

where Ψ_v is the vacuum flux and Ψ_FC is the flux from flux-conserving current loops, if any.

An initial guess for Ψ was determined heuristically. Equations (18) and (19) were successively applied to the existing j_ϕ and Ψ guesses until the variation was smaller than a tolerance. In this manner a self-consistent equilibrium was computed.

Useful Grad–Shafranov solvers must include the possibility that some axial field coils conserve magnetic flux. On a short timescale, all electrically conductive loops such as the vacuum vessel wall will conserve flux. On a long timescale, any superconducting coils operating in a persistent mode will conserve flux.

For computations including flux conserving current loops, the flux conserver (FC) current I_FC was determined using the equation

$$\vec{I}_\mathrm{FC} = M^{-1} \vec{\Psi}_\mathrm{P,FC}, \tag{20}$$

where $\vec{I}_\mathrm{FC}$ is the list of FC currents, $\vec{\Psi}_\mathrm{P,FC}$ is the list of plasma fluxes computed from j_ϕ evaluated at the FC locations, and M is the matrix of mutual- and self-inductances between the flux conserving loops.

The function $\partial_\Psi P(\Psi)$ in equation (18) comes from either equations (12) or (15) (if isothermal). Both of these equations have a free multiplicative factor. This factor can be assumed, or can be used to satisfy a useful constraint, such as a location that lies upon the separatrix or the maximum value of the flux. If this approach is to be used, the value of the free factor is set every iteration after equation (18) is applied, by enforcing the constraint. Other constraints might be: diamagnetic loop measurement constrained to be a specific value, line-averaged density constrained to be a specific value, maximum flux constrained to be a specific value, etc.

Any configuration of axial field coils (producing Ψ_v) and flux-conserving loops (producing Ψ_FC) may be used. Each corresponds to a different experiment or reactor. For generality, the results given in this paper are for constant vacuum mag-

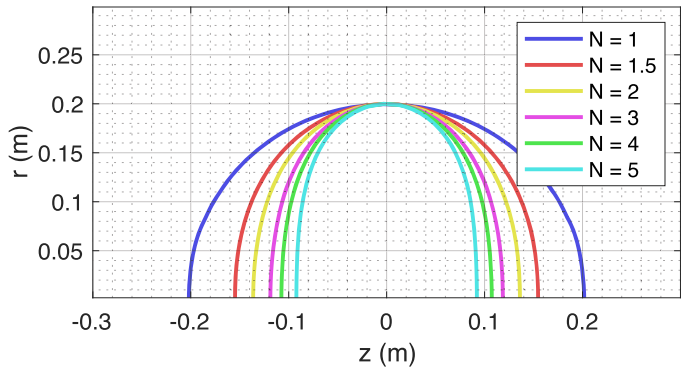

Figure 3. FRC separatrices for various values of N, where $P \propto \Psi^N$. Different values of N correspond to different relative peakednesses of density and temperature.

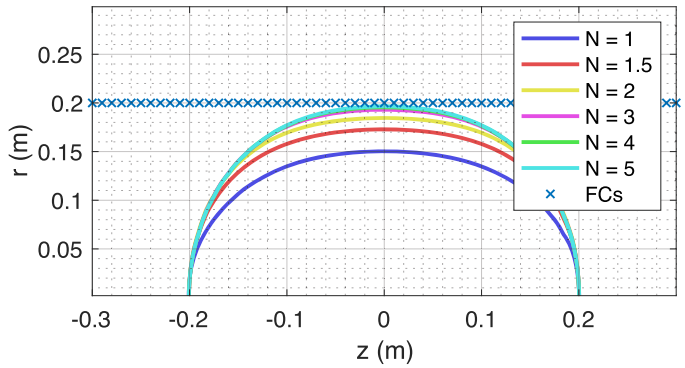

Figure 4. FRC separatrices for various values of N. A barrier of flux-conserving loops has been placed at $r = 20$ cm. These flux conservers (FCs) are able to counteract the tendency for the FRC to become oblate.

netic field, $\Psi_v \propto r^2$, and unless otherwise stated there were no flux conserving loops.

8. Results

8.1. The case of $0 \leqslant \mu < 1$

Several equilibria were found for various $N = \frac{1}{1-\mu}$ values, corresponding to various dependencies of the density and temperature on the pressure. $N = 1$ corresponds to the constant-density, varying-temperature case, and the Solov'ev solution is recovered. As N increases, the density profile becomes more and more peaked compared to the temperature profile.

The equilibria were computed assuming a uniform vacuum field of 5 T and an RMF frequency of $2\pi \times 0.5 \times 10^6$ rad s^{-1}. The separatrix radius was constrained to be 20 cm.

Increasing oblateness: figure 3 shows the separatrices of FRCs calculated with several values of N. $N = 1$ corresponds to the Solov'ev case, and a spherical Hill's vortex is recovered. As N increases, the separatrix becomes more and more oblate.

This oblateness can be mitigated with the use of flux conserving current elements in close proximity to the FRC. Another set of solutions is depicted in figure 4. The difference is that a cylindrical shell of closely spaced, flux conserving loops was placed around the plasma, constraining its radial growth. For these solutions, the X-point was constrained to lie at 20 cm. As can be seen in that figure, FCs are able to keep the FRC prolate. By tailoring the placement of axial field coils and flux conserving loops, it is possible to control the shape of the plasma separatrix.

Yet another set of solutions is depicted in figure 5. This set of solutions keeps $N = 3$ and varies the Ψ_0 parameter in equation (12), the flux limit outside of which the density and temperature are zero. As density and temperature is allowed to exist outside the separatrix (Ψ_0 becomes negative), the separatrix becomes less oblate and more prolate. However, there is significant density outside the FRC, where plasma is less well confined and it can hit the walls or flow to a divertor or end cell. The flux limit, Ψ_0, is shown in figure 6. As Ψ_0 becomes more negative, more of the plasma is in the open field line region and approaches the wall of the vacuum vessel.

It may be that transport requires $\Psi_0 < 0$ in experiments and reactors. This would mean that there is always some amount of plasma outside the separatrix, in the open field line region. Confinement is poorer in the open field line region. It is mirror confinement rather than cross-field confinement, causing axial losses. Some implications of this are discussed briefly in section 9.

Increasingly peaked density: figure 7 shows the radial profile of the density $n(r)$ at $z = 0$. For the $N = 1$ case, the density is constant as was assumed. As N increases, the maximum

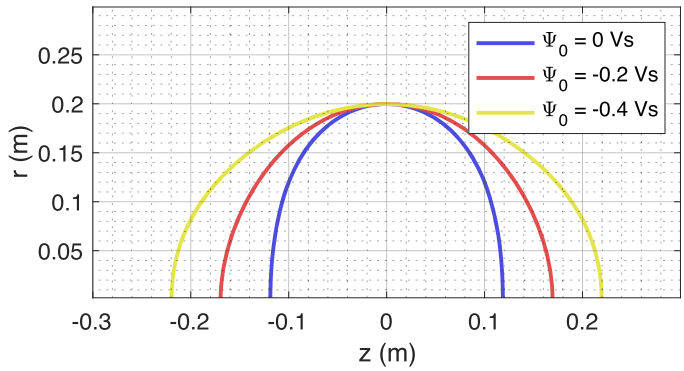

Figure 5. FRC separatrices for $N = 3$. Various values of the limiting flux Ψ_0 are used. Outside this flux, $n, T = 0$. As plasma is allowed to exist outside the separatrix (Ψ_0 becomes negative), the separatrix becomes less oblate. Ψ_o is given in units of volt-seconds (Vs).

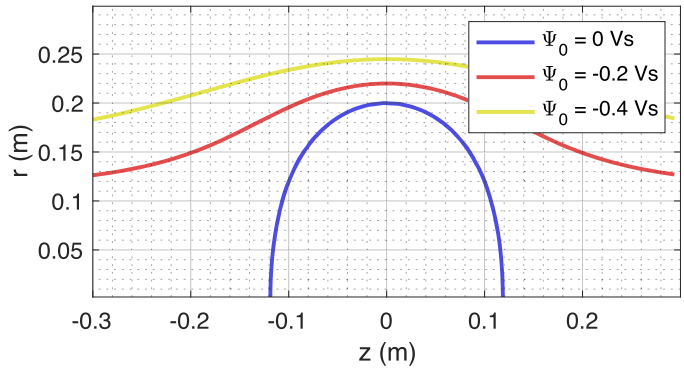

Figure 6. The same equilibria as figure 5. The spatial location at which Ψ_0 is reached for various values of Ψ_0. Outside these contours, $n, T = 0$. As Ψ_0 becomes more negative, the plasma persists farther outward of the separatrix. Ψ_o is given in units of volt-seconds (Vs).

density grows larger and the density profile becomes more peaked and narrow.

As discussed in section 4, at some point the increasing density will cause imperfect penetration of the RMF, saturating the effect and limiting the density peakedness.

The fact that the density is more peaked is not of itself useful. We will compute its effect on the volume-averaged pressure and a quantity relevant to fusion power density in the next subsections. Surprisingly, locally the density profile is so peaked that $\beta \gg 1$ over a small volume.

Increasingly peaked temperature: figure 8 shows the radial profile of the temperature $T(r)$ at $z = 0$. Recall that $T = T_e + T_i$ as defined in equation (9). For the $N = 1$ case, the temperature is proportional to the flux Ψ. As $N > 1$, $T(r)$ becomes more peaked, though less so than $n(r)$.

This is a surprising result. One might instead expect $T(r)$ to become less peaked as N increases, as the dependence of temperature on pressure $T(P)$ becomes less steep as per equation (11). However, as N increases the pressure flux function $P(\Psi)$ becomes steeper as per equation (12). The net effect is that the pressure profile $P(r)$ as determined via Picard iteration becomes steeper faster than the temperature dependence on pressure $T(P)$ becomes shallow, and the net effect is that the temperature profile $T(r)$ becomes more steep.

Decreasing volume-averaged plasma pressure: figure 9 shows the plasma pressure P, averaged over a cylinder with the radius of the separatrix and the half-length of the radius of the separatrix (20 cm). While the maximum density clearly increases, as can be seen in figure 7, it is squeezed into an ever smaller volume, and so the volume-averaged pressure decreases. Consequently the FRC has a lower volume-averaged pressure ratio, $\langle\beta\rangle$, at higher N. This may at first seem deleterious to a fusion reactor. However, the fusion power density is not proportional to plasma pressure P; rather it is proportional to n^2 with a highly nonlinear function of T.

In this paper, β is evaluated as the volume-averaged plasma pressure over the volume averaged *vacuum* magnetic pressure,

$$\langle\beta\rangle \equiv \frac{\int \mathrm{d}V nT}{\int \mathrm{d}V B_0^2/2\mu_0}, \tag{21}$$

where $\int \mathrm{d}V$ is the integral over the specified volume and B_0 is the vacuum magnetic field.

Increasing volume-averaged square pressure: figure 10 shows the square plasma pressure, $\langle n^2T^2\rangle$, averaged over a cylinder with the radius of the separatrix and the half-length of the radius of the separatrix (20 cm). It is an increasing function of N. In the balance between increasing density and decreasing volume, the increasing density wins out and the quantity increases.

These values of $\langle n^2T^2\rangle$ were generated using $\omega_e = 0.5 \times 2\pi \times 10^6$ rad s^{-1}. Flux field Ψ and pressure P were produced via Picard iteration. Temperature is specified per equation (14),

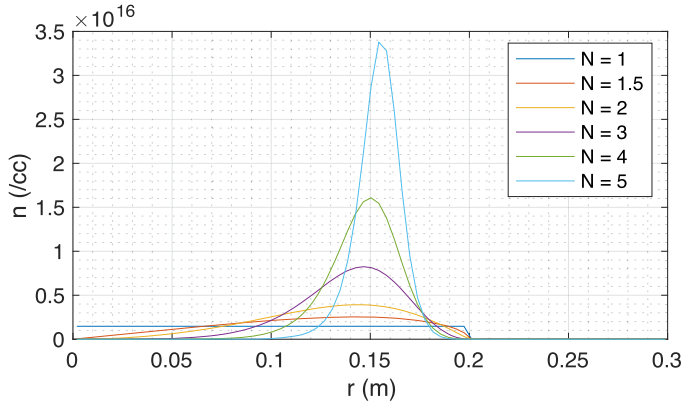

Figure 7. The same equilibria as figure 3. Radial profiles of density $n(r)$ at the $z = 0$ plane for various values of N. As N increases, the density profile becomes more peaked and the maximum density increases. We have assumed that $n_e = n_i = n$.

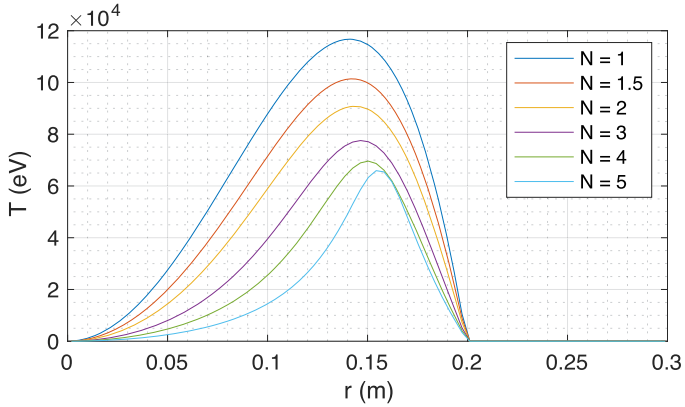

Figure 8. The same equilibria as figure 3. Radial profiles of temperature $T(r)$ at the $z = 0$ plane for various values of N. As N increases, the temperature profile becomes more peaked and the maximum temperature decreases. These high temperatures, $T > 100$ keV, are relevant to advanced fuels such as D + ^{3}He.

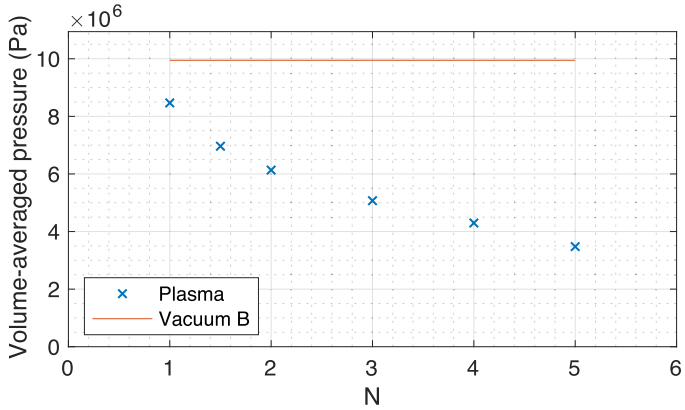

Figure 9. The same equilibria as figure 3. These are the volume-averaged plasma pressure for various values of N. The volume was taken to be a cylinder with radius $r = 20$ cm, the separatrix radius, and $L = 40$ cm long. Recall there is no plasma outside the separatrix in these equilibria. The volume-averaged pressure decreases with increasing N.

which then specifies density n via the pressure relationship, equation (7). Recall that ω_e is essentially a free parameter. Thus, ω_e could be set (by setting ω_{RMF}) so that T_{max}, the maximum temperature, were constant in N.

At high N, density is much more peaked than T. We can therefore approximate $T \approx T_{max}$ as constant over the region of high n^2. Applying the procedure in the preceding paragraph (T_{max} constant), this quantity $\langle n^2 T^2 \rangle \approx T_{max}^2 \langle n^2 \rangle \propto n^2$ therefore approximates the fusion power density.

The results in figure 10 indicate that the fusion power output from a Rotamak-FRC whose temperature is more constant than its density ($\mu > 0.5$) can be higher than the power

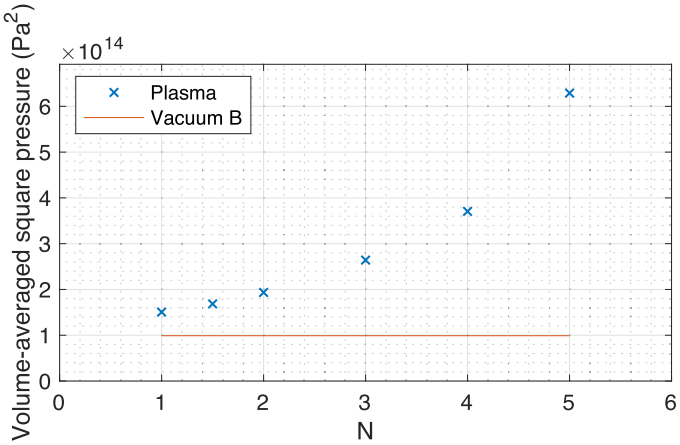

Figure 10. The same equilibria as figure 3. These are the volume-averaged square plasma pressure for various values of N. The volume was taken to be a cylinder with radius $r = 20$ cm, the separatrix radius, and $L = 40$ cm long. The volume-averaged square pressure increases with increasing N. Recall there is no plasma outside the separatrix in these equilibria. The volume-averaged square pressure is a good approximation for the fusion power when the maximum temperature is constant and the temperature profile is less peaked than the density profile.

Table 2. Summary of the results of figures 9 and 10. The $N = 0$ case is the result of a point-plasma model, where the pressure was calculated from $\beta = 1$ in the 5 T vacuum field. The $N = 1$ case is the commonly assumed Solov'ev solution, the Hill's vortex. F is $\langle\beta^2\rangle$, which approximates the enhancement to the fusion power as a result of density peakedness. N is a measure of the relative peakedness of the density and temperature; $N > 1$ is likely in reactor-scale experiments as discussed in section 6.

N	$\langle P\rangle$ (MPa)	$\sqrt{\langle P^2\rangle}$ (MPa)	F^a
0[b]	9.95	9.95	1
1[c]	8.47	12.3	1.52
1.5	6.96	13.0	1.70
2	6.13	13.9	1.96
3	5.07	16.3	2.67
4	4.30	19.2	3.74
5	3.48	25.1	6.36

[a]Approximate fusion power enhancement factor, $\langle\beta^2\rangle$.
[b]Point-plasma model. Uniform pressure, $\beta = 1$ in 5 T vacuum field.
[c]Solov'ev solution, Hill's vortex.

output from an equivalent volume of plasma with $\beta = 1$ (plasma pressure over vacuum field). The concentration of density into a peaked structure is responsible for this result.

Summary table: a summary of these results is shown in table 2. They are compared to a case called $N = 0$ but is simply the result of a point-plasma model where $P = nT$ is determined from $\beta = 1$ in the 5 T vacuum field. For more peaked density than temperature, which is likely for reactor-scale plasmas, the fusion power output can be much higher than the equivalent volume of $\beta = 1$ plasma. β is calculated with respect to the vacuum field as per equation (21).

8.2. The isothermal case, $\mu = 1$

In this section we will discuss the special case of an isothermal plasma, $\mu = 1, N = \infty$.

The isothermal equilibria are characterized by the parameter Ψ_c in equation (15). Several equilibria were found for various $\Psi_c = \frac{2\pi T}{e\omega_e}$ values, corresponding to various temperatures and RMF frequencies.

The equilibria were computed assuming a uniform vacuum field of 5 T and a temperature of 50 keV. The separatrix radius was constrained to be 20 cm. The values of $\Psi_c = [0.115, 0.130, 0.200]$ Vs correspond to RMF angular frequencies of $\omega_e = [2.73 \times 10^6, 2.42 \times 10^6, 1.57 \times 10^6]$ rad s^{-1} respectively.

Values of Ψ are given in Vs, or volt-seconds.

Values of Ψ_c less than 0.115 Vs produced numerical problems, as the discretization of the grid (8 mm) was too large, so these equilibria could not be computed accurately. As discussed in section 4, at some point the increasing density may cause imperfect penetration of the RMF, possibly affecting the density peakedness.

Prolate and oblate separatrix: figure 11 shows the separatrices for various values of Ψ_c. The FRC can be either naturally oblate or naturally prolate, depending on the value of Ψ_c. As with the non-isothermal case, the shape of the FRC can also be manipulated with flux conserving or current-carrying coils (not shown).

Peakedness of density: figure 12 shows the radial density profiles $n(r)$ along the $z = 0$ line for various values of Ψ_c. A small Ψ_c corresponds to a high maximum density and a peaked spatial profile. A large Ψ_c corresponds to a low maximum density and a broad spatial profile.

As discussed in section 4, at some point the increasing density will cause imperfect penetration of the RMF, saturating the effect and limiting the density peakedness.

As discussed in section 8.1, this density peakedness also implies a higher fusion rate. As Ψ_c decreases (ω_e increases), the density profile becomes more and more peaked, decreasing $\langle\beta\rangle$ but increasing $\langle\beta^2\rangle$, which corresponds to fusion reaction rate. This is shown in figure 13. At $\Psi_c = 0.115$ Vs, the numerical stability limit for the resolution used (8 mm), the fusion rate is enhanced a factor of 2.5 over a $\beta = 1$ uniform plasma volume. As with the non-isothermal case, more peaked implies more fusion.

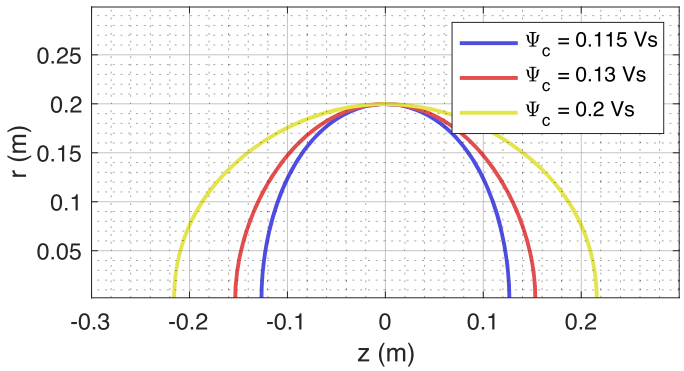

Figure 11. FRC separatrices for various values of Ψ_c, where $P \propto e^{\Psi/\Psi_c}$. Different values of Ψ_c correspond to different values of T, ω_e. As Ψ_c decreases (T decreases or ω_e increases), the FRC becomes more oblate. Ψ_c is given in units of volt-seconds (Vs).

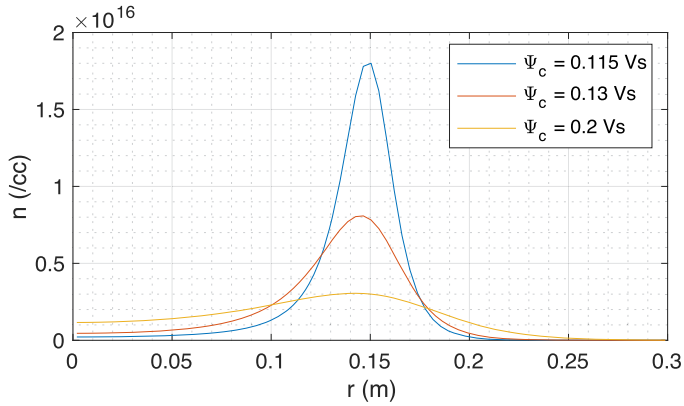

Figure 12. The same equilibria as figure 11. Radial profiles of density $n(r)$ at the $z = 0$ plane for various values of Ψ_c. As Ψ_c decreases, the density profile becomes more peaked and the maximum density increases. Locally, this highly peaked density can cause small volumes of $\beta \gg 1$. We have assumed that $n_e = n_i = n$. Ψ_c is given in units of volt-seconds (Vs).

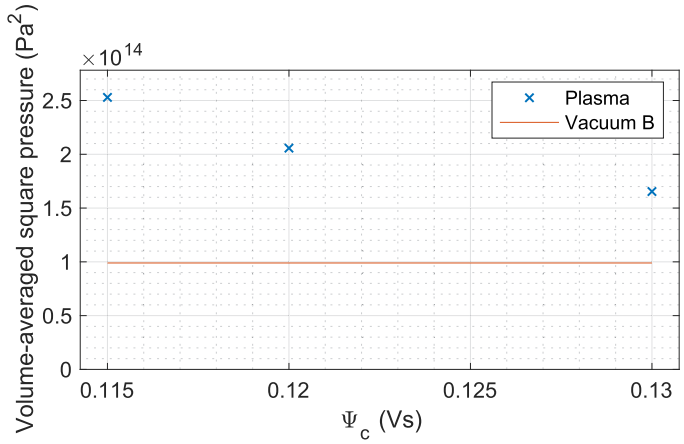

Figure 13. A set of isothermal equilibria with differing Ψ_c. These are the volume-averaged square plasma pressure. The volume was taken to be a cylinder with radius $r = 20$ cm, the separatrix radius, and $L = 40$ cm long. The volume-averaged square pressure decreases with increasing Ψ_c. The volume-averaged square pressure is proportional to the fusion power when the temperature is constant. Ψ_c is given in units of volt-seconds (Vs).

Density fall-off outside the separatrix: recall from section 5.4 that $n(r) \to 0$ is not compatible with isothermal rigid rotation. Thus, density is nonzero outside the separatrix. Figure 14 shows the contours in space where the density falls below 10^{14} 1/cm^3. For small Ψ_c, the exponential fall-off is sufficient to reduce the density to below 10^{14} 1/cm^3 in a short distance from the separatrix. As Ψ_c grows larger, the density profile broadens and the walls must be placed farther and farther away.

Confinement is poorer in the open field line region. It is mirror confinement rather than cross-field confinement, causing axial losses. Some implications of this are discussed briefly in section 9.

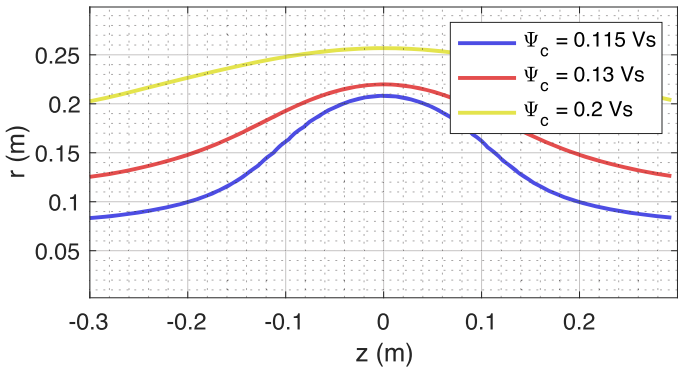

Figure 14. The same equilibria as figure 11. These are the contours at which $n_e = 10^{14}$ 1/cm^3. This indicates that the high density region extends farther toward the wall of the vacuum vessel when Ψ_c increases. Ψ_c is given in units of volt-seconds (Vs).

9. Discussion and conclusion

We have determined that fully co-rotating RMF-driven Rotamak-FRC experiments and reactors could beneficially have much more sharply peaked density profiles than a Hill's vortex, the Solov'ev solution. This is because the temperature profile is likely to be broader than the density profile, which together with rigidly rotating electrons implies a sharper functional form of the Grad–Shafranov pressure flux function. This entails both benefits and challenges to the creation of a compact fusion reactor.

One benefit is that the peakedness of the density profile enables a substantial increase in the total fusion power of the reactor, even while decreasing the $\langle\beta\rangle$. This increase may be ~ 5–$10\times$ depending on the relative broadness of the temperature and density.

One challenge is that the separatrix of the FRC tends to be naturally oblate. Oblateness can be controlled by separatrix shaping from current-carrying or flux-conserving coils around the FRC. Oblateness may also be reduced by allowing there to be significant plasma density outside the FRC, in the open field line region.

Another challenge is that density outside the FRC may be unavoidable. This model does not include field-parallel flows and mirror loss-cone losses, but this model does suggest that there may be significant density outside the separatrix.

This model allows RMF to produce arbitrarily peaked density profiles at high RMF frequencies. In this case, the model must break down as RMF penetration is imperfect at high densities and high collisionality. This must be an area of future exploration.

In the case of incompletely penetrated plasma, rigid rotation may only hold up to a certain flux contour. Alternatively, the entire FRC may spin at the same rate regardless of RMF penetration [17]. This case is not explored in this analysis, but one might expect a piecewise flux function in this case, where fluxes smaller than the penetration flux have the dependence given in equation (12) or (15), and fluxes larger than the penetration flux have some shallower dependence.

One could decouple the synchronous RMF frequency and the RF frequency by using a high-azimuthal-mode-number RMF antenna. Azimuthal mode number refers to

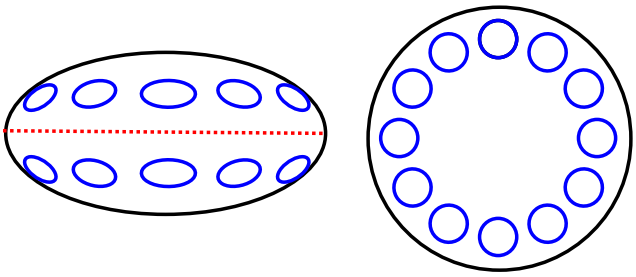

Figure 15. Location of odd-parity RMF antennae leaning into the oblateness of the FRC. Black: vacuum vessel. Red dashed line: vessel equator. Blue circles: RMF antennae. Left: side view, $\hat{z}$-axis points upward. Right: top view, $\hat{z}$-axis points out of the page.

$\vec{B}_{\hat{r},\hat{\phi},\mathrm{RMF}} \propto e^{im\phi}$, where m is the azimuthal mode number. $m = \pm 1$ is a straight field, which existing RMF antennae produce. $m = \pm 2$ would be a quadrupole field. $|m| > 1$ fields vanish at $r = 0$. Consider a point of constant RMF phase. It takes this point m RF periods to make one revolution of ϕ, so the RMF-synchronous frequency is a factor of m smaller than the RF frequency.

An intriguing possibility arises from leaning into the natural oblateness of FRCs with peaked spatial density profiles. This may be a novel and interesting parameter regime for later study. RMF coils facing axially, or a combination of axially and radially, rather than radially are naturally odd-parity, see figures 15 and 16, and the lower aspect ratio of this configuration gives plenty of space to include antennae at multiple azimuthal locations for high-mode-number RMF antennae. The coils would be roughly circular, flush with the oblate vacuum vessel, and spaced azimuthally. This would allow the radial profile of the RMF to be tailored. It would also allow a decoupling of the applied RF and synchronous rigid rotation frequencies.

Acknowledgments

We wish to acknowledge Bruce Berlinger for his work on the hardware of the PFRC-2 experiment. We wish to acknowledge graduate students Eugene Evans and George Constantinos for helpful discussions. We acknowledge Stephanie

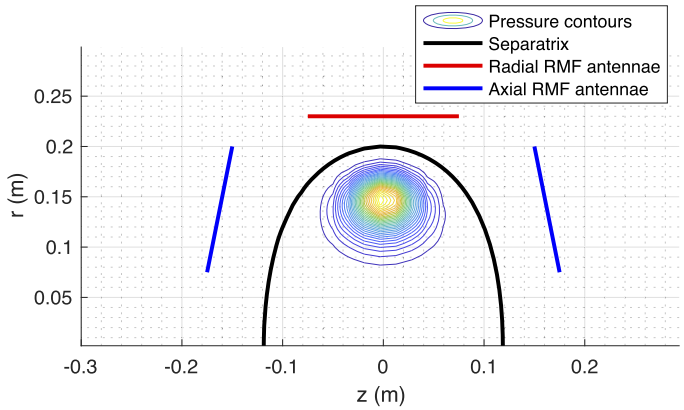

Figure 16. An equilibrium with $N = 3$ showing an oblate separatrix and peaked pressure profile, revealed by localized pressure contours. Red: the location of a traditional RMF antenna, even- or odd-parity, producing a radial RMF magnetic field. Blue: the location of RMF antennae leaning into the natural oblateness of the FRC, producing axial RMF magnetic fields. These are naturally odd-parity if the antennae have the same axial polarity. The axial RMF antennae are shown tilted to show that they can have some radial component and still produce useful and odd-parity fields.

Thomas and Michael Paluszek for contributing to the PFS Fusion Energy Toolbox. This work was supported by DOE contract DE-AR0001099, and in part by the Program in Plasma Science and Technology, DOE contract DE-AC02-09CH11466, NASA contract 80NSSC18C0218, and NASA contract 80NSSC18K0040.

ORCID iDs

C.P.S. Swanson https://orcid.org/0000-0003-0231-8525
S.A. Cohen https://orcid.org/0000-0002-8500-5526

References

[1] Hoffman A.L., Guo H.Y., Miller K.E. and Milroy R.D. 1994–2006 Principal physics of rotating magnetic-field current drive of field reversed configurations *Phys. Plasmas* **13** 012507
[2] Cohen S.A. *et al* 2019 Direct fusion drive for interstellar exploration *J. Br. Interplanet. Soc.* **72** 38–50
[3] Wurden G.A., Weber T.E., Turchi P.J., Parks P.B., Evans T.E., Cohen S.A., Cassibry J.T. and Campbell E.M. 2016 A new vision for fusion energy research: fusion rocket engines for planetary defense *J. Fusion Energy* **35** 123–33
[4] Cohen S.A. *et al* 2015 Reducing neutron emission from small fusion rocket engines 2015/10/16 IAC-15,C4,7-C3.5,9,x28852 Jerusalem, Israel *66th International Astronautical Congress*
[5] Slough J. and Miller K. 1999 FRC fusion propulsion system for deep space exploration results from the star thrust experiment (STX) *35th Joint Propulsion Conf. and Exhibit* (American Institute of Aeronautics and Astronautics)
[6] Miller K., Slough J. and Hoffman A. 1998 An overview of the star thrust experiment *AIP Conf. Proc.* **420** 1352–8
[7] Blevin H.A. and Thonemann P.C. 1962 Plasma confinement using an alternating magnetic field *Nuclear Fusion* (Abingdon, UK: Culham Laboratory) Suppl.
[8] Jones I., Turley M., Wedding J., Durance G., Hogg G. and Tendys J. 1987 An experimental investigation of low power, long duration Rotamak discharges *Aust. J. Phys.* **40** 157–74 Publisher: Csiro Publishing
[9] Hoffman A.L., Guo H.Y., Slough J.T., Tobin S.J., Schrank L.S., Reass W.A. and Wurden G.A. 2002 The TCS rotating magnetic field FRC current-drive experiment *Fusion Sci. Technol.* **41** 92–106
[10] Jones I.R. 1999 A review of rotating magnetic field current drive and the operation of the Rotamak as a field-reversed configuration (Rotamak-FRC) and a spherical tokamak (Rotamak-ST) *Phys. Plasmas* **6** 1950
[11] Cohen S.A., Berlinger B., Brunkhorst C., Brooks A., Ferraro N., Lundberg D.P., Roach A. and Glasser A.H. 2007 Formation of collisionless high-β plasmas by odd-parity rotating magnetic fields *Phys. Rev. Lett.* **98** 145002
[12] Cohen S., Brunkhorst C., Glasser A., Landsman A. and Welch D. 2011 RF plasma heating in the PFRC-2 device: motivation, goals and methods *AIP Conf. Proc.* **1406** 273–6 AIP Publishing
[13] Hugrass W.N. 1979 Production of plasma currents using transverse rotating magnetic fields *Thesis* Adel
[14] Hugrass W.N. and Grimm R.C. 1981 A numerical study of the generation of an azimuthal current in a plasma cylinder using a transverse rotating magnetic field *J. Plasma Phys.* **26** 455–64
[15] Jones I.R. and Hugrass W.N. 1981 Steady-state solutions for the penetration of a rotating magnetic field into a plasma column *J. Plasma Phys.* **26** 441–53
[16] Milroy R.D. 1994–1999 A numerical study of rotating magnetic fields as a current drive for field reversed configurations *Phys. Plasmas* **6** 2771–80
[17] Rostoker N. and Qerushi A. 2002 Equilibrium of field reversed configurations with rotation. I. One space dimension and one type of ion *Phys. Plasmas* **9** 3057–67 Publisher: American Institute of Physics
[18] Guo H.Y., Hoffman A.L. and Milroy R.D. 2007 Rotating magnetic field current drive of high-temperature field reversed configurations with high ζ scaling *Phys. Plasmas* **14** 112502
[19] Welch D.R., Cohen S.A., Genoni T.C. and Glasser A.H. 2010 Formation of field-reversed-configuration plasma with punctuated-betatron-orbit electrons *Phys. Rev. Lett.* **105** 015002
[20] Grad H. and Rubin H. 1954–1958 Hydromagnetic equilibria and force-free fields *J. Nucl. Energy* **7** 284–5
[21] Solov'ev L.S. and Shafranov V.D. 1970 Plasma confinement in closed magnetic systems *Reviews of Plasma Physics* (Berlin: Springer) pp 1–247

[22] Petrov Y., Yang X., Wang Y. and Huang T.-S. 2010 Experiments on Rotamak plasma equilibrium and shape control *Phys. Plasmas* **17** 012506
[23] Euripides P., Jones I.R. and Deng C. 1997 Rotamak discharges in a 0.5 m diameter, spherical device *Nucl. Fusion* **37** 1505–8 Publisher: IOP Publishing
[24] Bellan P.M. 1989 Particle confinement in realistic 3D Rotamak equilibria *Phys. Rev. Lett.* **62** 2464–7
[25] Storer R.G. 1982 Pressure balance equilibria in the Rotamak *Plasma Phys.* **24** 543–54 Publisher: IOP Publishing
[26] Storer R.G. 1983 Compact torus equilibria set up in the Rotamak by rotating magnetic fields *Nucl. Instrum. Methods Phys. Res.* **207** 135–8
[27] Donnelly I., Rose E. and Cook J. 1987 Magnetohydrodynamic equilibrium models for Rotamak plasmas *Aust. J. Phys.* **40** 175–84 Publisher: Csiro Publishing
[28] Christofilos N.C. 1958 Astron thermonuclear reactor *Proc. 2nd United Nations Int. Conf. on the Peaceful Uses of Atomic Energy* vol 32 (Geneva, Switzerland) (United Nations) pp 279–90 Number: INIS-XU–022
[29] Marder B. and Weitzner H. 1970 A bifurcation problem in E-layer equilibria *Plasma Phys.* **12** 435–45 Publisher: IOP Publishing
[30] Armstrong W.T., Linford R.K., Lipson J., Platts D.A. and Sherwood E.G. 1981 Field-reversed experiments (FRX) on compact toroids *Phys. Fluids* **24** 2068–89 Publisher: American Institute of Physics
[31] Belova E.V., Jardin S.C., Ji H., Yamada M. and Kulsrud R. 2000 Numerical study of tilt stability of prolate field-reversed configurations *Phys. Plasmas* **7** 4996–5006 Publisher: American Institute of Physics
[32] Gota H., Fujimoto K., Ohkuma Y., Takahashi T. and Nogi Y. 2003 Separatrix shapes and internal structures of a field-reversed configuration plasma *Phys. Plasmas* **10** 4763–70 Publisher: American Institute of Physics
[33] Steinhauer L. 2014 Two-dimensional interpreter for field-reversed configurations *Phys. Plasmas* **21** 082516 Publisher: American Institute of Physics
[34] Hewett D.W. and Spencer R.L. 1983 Two-dimensional equilibria of field-reversed configurations in a perfectly conducting cylindrical shell *Phys. Fluids* **26** 1299–304 Publisher: American Institute of Physics
[35] Guo H.Y. *et al* 2008 Improved confinement and current drive of high temperature field reversed configurations in the new translation, confinement, and sustainment upgrade device *Phys. Plasmas* **15** 056101
[36] Rostoker N. and Qerushi A. 2003 Classical transport in a field reversed configuration *Plasma Phys. Rep.* **29** 626–30
[37] Binderbauer M.W. *et al* 2015 A high performance field-reversed configurational *Phys. Plasmas* **22** 056110
[38] Velas K.M. and Milroy R.D. 2014 Probe measurements of the three-dimensional magnetic field structure in a rotating magnetic field sustained field-reversed configuration *Phys. Plasmas* **21** 012502 Publisher: American Institute of Physics
[39] Steinhauer L.C. 2001 Transient and quasisteady behavior with rotating magnetic field current drive *Phys. Plasmas* **8** 3367–76 Publisher: American Institute of Physics
[40] Morse R.L. 1969 Equilibria of collisionless plasma, part II *Technical Report LA-3844* Los Alamos Scientific Lab New Mexico
[41] Tuszewski M. 1988 Field reversed configurations *Nucl. Fusion* **28** 2033
[42] Hinton F.L. and Hazeltine R.D. 1976 Theory of plasma transport in toroidal confinement systems *Rev. Mod. Phys.* **48** 239–308
[43] Stangeby P.C. 2000 *The Plasma Boundary of Magnetic Fusion Devices* (London: Taylor and Francis) google-Books-ID: qOliQgAACAAJ
[44] Zakharov L.E., Li X., Galkin S.A. and Guazotto L. 2014 Li wall fusion—no alternative No other option (https://w3.pppl.gov/~zakharov/LEZ-140530.pdf)